Bimetallic Nano Electrocatalyst for HER in Alkaline Polymer Electrolysis

Alaa.Y.Faid[a], M.Mainkidan[a], Frode Seland[a], Alejandro Oyarce Barnett[b], Svein Sunde[a]

[a] Norwegian University of Science and Technology, Trondheim, Norway
[b] SINTEF Materials and Chemistry, Norway

Ni and alloys of Ni (with Fe, Co, Mo) still represent the most suitable electrodes for HER in alkaline media. Bimetallic nanoparticles of NiFe and NiCo were fabricated by co-precipitation and thermal reduction by oleylamine. The process of co-precipitation involves NaOH as a precipitation agent to precipitate the metal-based nitrates, while thermal reduction process involves the synthesis of metal-containing compounds using oleylamine, which act as reducing agent, surfactant, and solvent. Different synthesis conditions in terms of composition were studied. Structural characterization of nanoparticles was carried out using scanning electron microscopy, energy dispersive x-ray, X-ray diffraction, Raman spectroscopy and BET surface area. Electrochemical behavior of nanoparticles was investigated using rotating disk electrode. The electrochemical characterization studied the effect of catalyst composition on the electrochemical behavior of the catalyst.

Introduction

The Polymer Electrolyte Membrane electrolyzer (PEMEL) has attracted considerable attention during the last decades. Some of the advantages of PEM electrolysis are i) high current densities due to low parasitic energy losses, ii) rapid power-up/power-down rates and iii) high purity and high-pressure hydrogen. PEMELs are therefore promising devices to produce hydrogen for energy storage purposes and use in the transport sector. The low pH associated with these devices results in fast hydrogen evolution reaction (HER) at the cathode (1). Alkaline water electrolyzers with aqueous electrolytes represent the classical technology for water electrolysis which operating at a high pH. Although the overpotential for oxygen evolution reaction (OER) at the anode is larger compared to that of the HER at the cathode, the OER overpotential is still low compared to the case of PEM (acid environment). The overpotentials associated to the HER at the cathode have been reported to be exceptionally high compared to low pH, a hundred-fold decrease in activity at Pt, Ir, and Pd (2).

Recent developments in alkaline membrane technology have led to the possibility of using anion-exchange membranes containing alkaline ions (OH^-, CO_3^{2-}, HCO_3^-) in water electrolysis. This technology has the potential of combining the advantage of non-precious catalysts of the alkaline process, with the advantages of PEMEL, e.g. fast power-up/power-down rates, low parasitic energy losses, and low energy consumption, in other words consolidating the best of both technologies (3).

The hydrogen binding energy can be considered as the primary descriptor of catalytic activity under alkaline conditions. The reason for the lower activity has been suggested to be a stronger bond between the hydrogen and the metal surface under alkaline conditions, which may account for as much as a factor 200 decreasing in activity (4). The fact that hydrogen binding energy is a good descriptor of electrocatalytic activity at high pH, which makes the catalysts subject to rational design guided by the d-band theory for transition metal electrocatalysis (5). Catalyst particle size should also be considered in the rational design of hydrogen evolution or oxidation catalyst. Small particles will possess several sites with coordination numbers smaller than those at the corresponding bulk surfaces. Adsorption at these low coordination sites has recently been shown to strengthen the bond between the adsorbate and the site (5).

Electrocatalysts based on transition metal oxides (TMOs) are well known to be cheap, environmentally favorable and active OER catalysts in alkaline environments. Therefore, development of oxide-based alkaline HER catalysts will boost the bifunctional activity of these oxides, which is beneficial for overall water splitting application (6). Electron densities of low coordinated oxygen (LCO) in metal oxides have been reported from recent studies. It is found that the atoms on the surface of metal oxides are lower than those in regular sites in the bulk, demonstrating the presence of active non-bonding states for the adsorption of H_{ad} (7). Moreover, poor intrinsic electronic conductivity is another fundamental issue that restricts activity enhancement of TMO-based catalysts. Coupled nickel oxide with conductive carbon nanotubes forming hybrid catalysts to enhance the conductivity of the catalysts. Nevertheless, fundamental knowledge of hydrogen evolution mechanism on TMOs is still unclear (8). Simply fabricated, and stable spinel transition metal oxides (TMOs) are considered appropriate candidates for HER. Further, one of the remaining challenges in the fields of chemistry, materials, and the hydrogen energy industry is to develop highly efficient HER electrocatalysts capable to work at high current densities.

In this work, a detailed study was carried out on NiFe and NiCo catalyst with a different composition. Investigation of the composition effect on activity has been illustrated based on the analysis of surface morphology, crystalline phases, and BET surface area. A trend of composition dependence of preferable spinel oxide phase has been demonstrated. The relationship between the composition of nanoparticles and the catalytic activity for HER was illustrated.

Experimental Methods

Preparation of the catalyst

Co-precipitation: NiFe and NiCo based oxides were fabricated by typical co-precipitation method. Appropriate molar concentrations of as-received $Ni(NO_3)_2.6H_2O$ (Sigma-Aldrich), $FeCl_3.6H_2O$ (Sigma-Aldrich) (purity > 99.9%) and $Co(NO_3)_2.6H_2O$ (Sigma-Aldrich) were dissolved in 150 ml of deionized (DI) water under stirring for 15 min. Then 2 M NaOH solution was added under continuous stirring until precipitate formed. Precipitation occurs when the pH of the reaction mixture reaches value higher than 12. The solution was stirred for another hour at room temperature (22 ± 2 °C) and left to stand for 12 hours.

The precipitated solution was filtered, washed with DI water and dried at 80 °C. The hydroxide precipitate was moved to a crucible and calcinated at 500 °C for 4 h under 5% H_2 / 95 % Ar atmosphere.

Thermal reduction by oleylamine: For a typical synthesis, a mixture of 14 mL of oleylamine (Sigma-Aldrich), 6 ml of trioctylphosphine (TOP) (Sigma-Aldrich), 1 mmol of Nickel(II) acetylacetonate (Ni(acac)$_2$, 97%) (Sigma-Aldrich), 1 mmol of Cobalt(II) acetylacetonate (Co(acac)$_2$, 97%) (Sigma-Aldrich) and Iron(III) acetylacetonate (Fe(acac)$_3$, 97%) (Sigma-Aldrich) were transferred into a three-necked flask and kept under Ar gas flow. The mixture was degassed at 100 °C with continuous stirring under Ar gas flow. The produced solution was heated up to 210 °C and kept at this temperature for 45 min. After cooling down to room temperature, excess acetone was added to the black solution to give a black precipitate which was isolated via centrifugation (8500 rpm for 6 min). The final precipitate was washed with a mixture of hexane and acetone.

Preparation of the electrode for RDE measurement

For rotating desk electrode (RDE) experiments, a catalyst ink was prepared by homogenization of 5 mg of catalyst powder in a solution of (0.5 ml D.I water, 0.44 ml Isopropanol (Sigma Aldrich) + 60 µl Nafion 117 solution (Sigma Aldrich)- 5 wt % in a mixture of lower aliphatic alcohols and water) and ultrasonicated for 30 minutes. To investigate the electrocatalytic activity, an aliquot of 10 µL of homogenized catalyst ink was deposited by a micropipette on the cleaned and polished GC tip mounted on an inverted rotator shaft rotated at 200 rpm. The ink was subsequently dried in air at room temperature by increasing and maintaining the rotator speed at 700 rpm for 30 min.

Catalyst characterization

The morphology of the prepared powder samples was studied using scanning electron microscopy (SEM, Carl Zeiss supra 55) operated at a 10-kV accelerating voltage and Hitachi S500 STEM. Composition and elemental analysis were carried out using energy dispersive spectroscopy (EDS) in SEM. Structural and phase characteristics of the catalyst were obtained by means of a Bruker D8 A25 DaVinci X-ray Diffractometer with $Cu_{K\alpha}$ radiation. The wavelength of the radiation was 1.5425 Å. Diffractograms were taken between 15 [2θ] and 75 [2θ] using a step size of 0.3 [2θ]. The values of the unit cell dimension (a) and the crystallite size were determined by Rietveld analysis and linear broadening of the most intense diffraction peak present. Raman spectroscopy was performed with a Renishaw InVia Reflex Spectrometer System using VIS excitation at 532 nm (100mW) with spectral resolution < 1 cm^{-1} at room temperature (22 ± 2 °C). Catalyst specific surface area was determined using the Brunauer-Emmett-Teller method (BET) of nitrogen adsorption using a TRISTAR 3000 surface area and porosity analyzer. Samples were degassed at 250 °C under vacuum overnight prior to the measurement.

Electrocatalytic measurements

The electrochemical measurements, namely linear sweep voltammetry (LSV) was performed using an (Ivium-n-Stat) multi-channel electrochemical potentiostat-galvanostat. A conventional three-electrode arrangement was used.

A rotating disk electrode (RDE) (PINE MSRX rotator, PINE Research Instrumentation, USA), was used as a working electrode, Platinum foil served as a counter-electrode. A standard single junction mercury/mercury oxide (Hg/HgO) filled with a 4.24 M KOH solution was used as a reference electrode.

Freshly prepared nitrogen saturated 0.1 M KOH solutions were used as an electrolyte for each set of experiments. The 0.1 M KOH alkaline electrolyte was purged by N_2 gas for 30 minutes before the electrochemical measurements. The LSV curves were collected in a potential range of -0.8 to -1.9 V vs Hg/HgO using a scan rate of 5 mV s^{-1} at 1600 rpm rotation rate. All electrochemical experiments were carried out at a temperature of $(22 \pm 2 \,°C)$ and under ambient pressure. All resulting data were corrected for IR losses due to the solution resistance. The potential was corrected for ohmic resistance through the equation

$$E_{compensated} = E_{measured} - iR$$

where $E_{compensated}$ and $E_{measured}$ denote as the compensated and measured potentials, respectively.

Short-term stability tests were carried out using chronoamperometry. Electrochemical impedance spectroscopy (EIS) measurements were obtained in a frequency range from 0.01 Hz to 100 kHz in 0.1M KOH. All potentials measured were calibrated to RHE using

$$E_{RHE} = E_{Hg/HgO} + 0.0.098 \text{ V} + (0.059\text{V pH}).$$

where E_{RHE} is potential vs reversible hydrogen electrode and $E_{Hg/HgO}$ is potential vs mercury/mercury oxide.

Results and discussion

Figure 1 shows the surface morphology of NiFe and NiCo nanoparticles prepared by the co-precipitation method and calcined at 500 ºC for 4 h under 5% H_2/ 95 % Ar atmosphere. Figure 1.a and 1.b displays that the produced particles are homogenous with the estimated cluster size ranging between 140 ± 4.65 and 160 ± 3.24 nm. Particles are aggregated and agglomerated possibly during the calcination step of the preparation procedure. These morphological characteristics are found to be the same even with different Ni/Fe % and Ni/Co %. As shown in Figure 1.a, the prepared particles formed the cluster by the united particle. From this fact, these particles need grinding to use as a precursor for the electrode. similar results reported by Chanda et al (9).

Energy dispersive x-ray (EDX) was recorded to investigate the elemental composition of the sample. EDX analysis confirmed that the prepared material consists of Ni, Fe, O and Co, Ni, O respectively, without any incorporation of NO_3^- or Cl$^-$ ions. The results are shown in figure 1.c and 1.d for Ni/Fe % and Ni/Co % = 0.5. Based on this analysis, the molecular formula of the oxide catalyst component was found to be $Ni_{0.985}Fe_{2.015}O_4$ and $Ni_{1.03}Co_{1.97}O_4$ respectively.

Based on literature, formation of $Ni_xFe_{3-x}O_4$ and $Ni_xCo_{3-x}O_4$ nanoparticles carried out through the chemical reaction indicated (10): For example $NiCo_2O_4$:

$$Ni(NO_3)_2.6H_2O + Co(NO_3)_2.6H_2O + 6KOH \longrightarrow Ni(OH)_2 + Co(OH)_2 + 6\ KNO_3$$
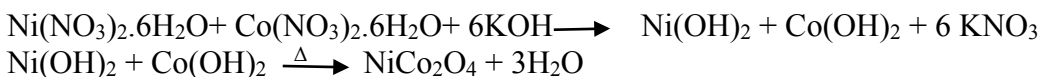$$Ni(OH)_2 + Co(OH)_2 \xrightarrow{\Delta} NiCo_2O_4 + 3H_2O$$

Table 1 shows Ni, Fe, Co and O % resulted from energy dispersive x-ray for designated $Ni_xFe_{3-x}O_4$ and $Ni_xCo_{3-x}O_4$ which in accordance with proposed oxide formulates.
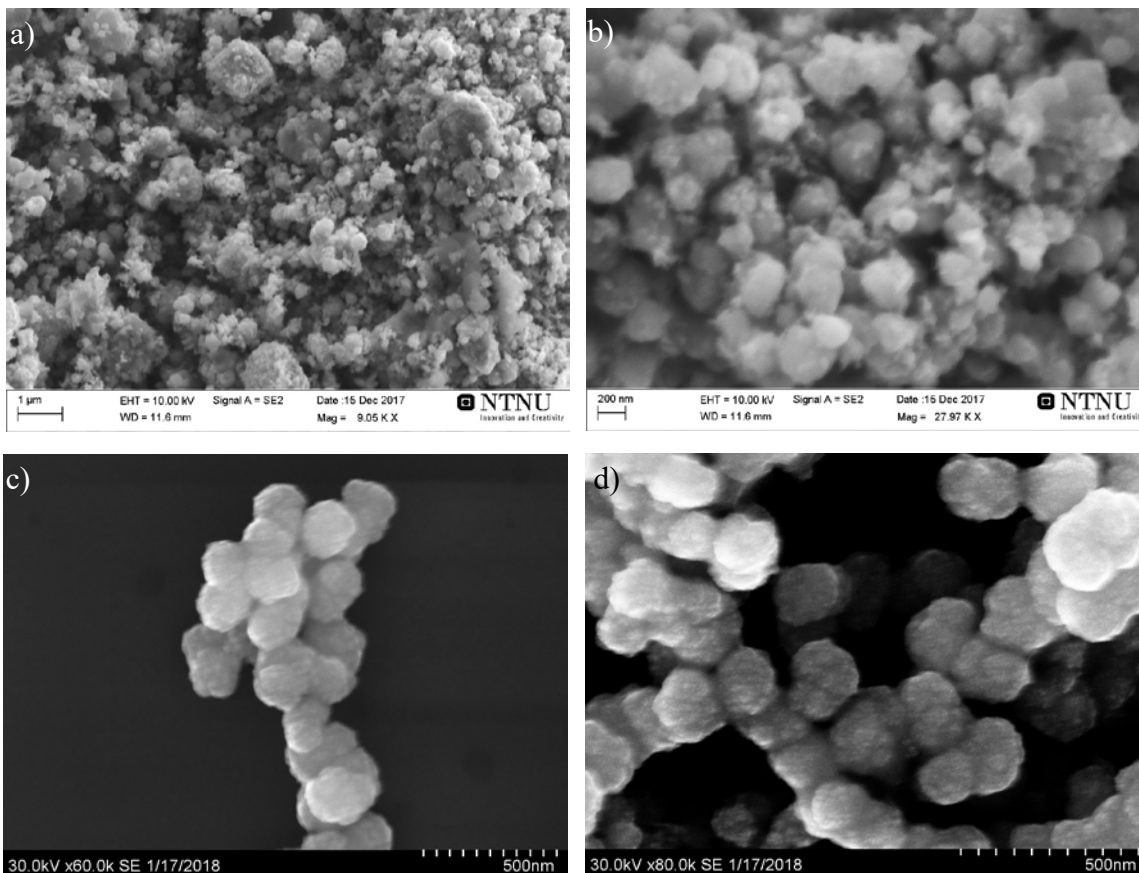
Figure 1 SEM image of a) $NiFe_2O_4$ and b) $NiCo_2O_4$ prepared by coprecipitation, and corresponding high magnification image of c) $NiFe_2O_4$ and d) $NiCo_2O_4$ sample.

Table 1 Overview of weight % of resulted NiFe and NiCo oxides synthesized by simple co-precipitation process.

Compound	Ni %	Fe %	Co %	O %
Fe_3O_4	0	42		58
$Ni_{0.25}Fe_{2.75}O_4$	8	70		22
$Ni_{0.5}Fe_{2.5}O_4$	15	65		20
$Ni_{0.75}Fe_{2.25}O_4$	20	57		23
$NiFe_2O_4$	27	50		23
NiO	48	0		52
Co_3O_4	0		43.3	56.7
$Ni_{0.25}Co_{2.75}O_4$	9		68	23
$Ni_{0.5}Co_{2.5}O_4$	13		56	21
$Ni_{0.75}Co_{2.25}O_4$	18.5		59	22.5
$NiCo_2O_4$	27		51	22

Structural characterization and crystallinity of the material were performed by X-ray diffraction (XRD). XRD pattern obtained from NiFe samples is shown in Figure 2.a. The diffraction peaks at 2θ values of 30.11°, 35.57°, 43.11°, 48.2°, 53.33°, 57.11° and 63.21° can be attributed to the crystalline planes of (220), (311), (400), (441), (422), (511), (440) respectively of $Ni_xFe_{3-x}O_4$. It could be seen that the diffraction peaks assigned to the spinel-type of $NiFe_2O_4$ with JCPDS no.86-2267 (11,12). While for NiO particles, the peak position appearing at 2θ = 43.3° can be indexed to (200) reflection of face-centered cubic (fcc) NiO. XRD pattern of Fe_3O_4 nanoparticles is shown in the Fig 2.a The peaks at 2θ values of 32.32°, 35.4°, 43.38°, 53.36°, and 63.12° are indexed as the diffractions of (311), (222), (422), (511) and (440) respectively, which indicate the standard diffraction spectrum of Fe_3O_4 (JCPDS no.19-0629) (13,14).

Figure 2.b shows the XRD pattern of the $Ni_xCo_{3-x}O_4$ catalyst synthesized by coprecipitation. the peak positions appearing at around 18.98°, 31.27°, 36.91°, 44.17°,45.2°, 59.35°, 62.3°, 64.82° can be indexed as (111), (220), (311), (222) (400), (422), (511), and (440) crystal planes of $NiCo_2O_4$. All diffraction peaks can be indexed to cubic spinel structure of $NiCo_2O_4$ (JCPDS; 73-1702) (6). No other peaks from any impurity were observed, indicating the high purity of the as-prepared $NiCo_2O_4$ nanoparticles. XRD patterns in Figure 2.b clearly show the development of (220) and (400) reflections when Ni/Co% exceeds 0.2%. The peak shift indicating substitutional incorporation of Ni into the Co_3O_4 structure. Co_3O_4 exhibits diffraction peaks with 2θ values at 29.37°, 37.02°, 43.57°, 64.44°. These diffraction peaks can be indexed to the crystalline cubic phase Co_3O_4 (JCPDS Card No76–1802) (14,15).

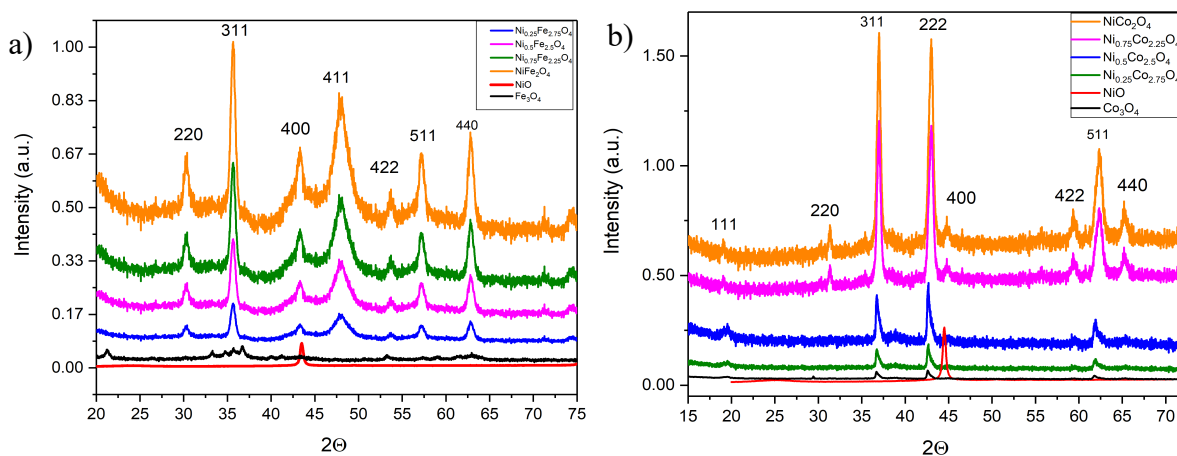Figure 2 XRD Pattern of a)$Ni_xFe_{3-x}O_4$ and b)$Ni_xCo_{3-x}O_4$, varying x from 0 to 1, catalyst powder prepared using co-precipitation with NaOH as precipitating agent and annealing in reducing atmosphere 5% H_2 / 95% Ar at 500 °C for 4 hours.

The lattice constant of the crystal structure was determined by Rietveld analysis of the XRD spectrum. In Figure 3.a, the calculated lattice constant of $Ni_xFe_{3-x}O_4$ was found to vary from 4.2 Å for NiO till 11.4 Å for Fe_3O_4, also changes in lattice constant in $Ni_{0.25}Fe_{2.75}O_4$ with increasing Ni/Fe% due to doping and substitution effect (9). The crystallite size calculated by XRD analysis of $Ni_xFe_{3-x}O_4$ was in the range of 18-31 nm which in good agreement with the previous literature (11).
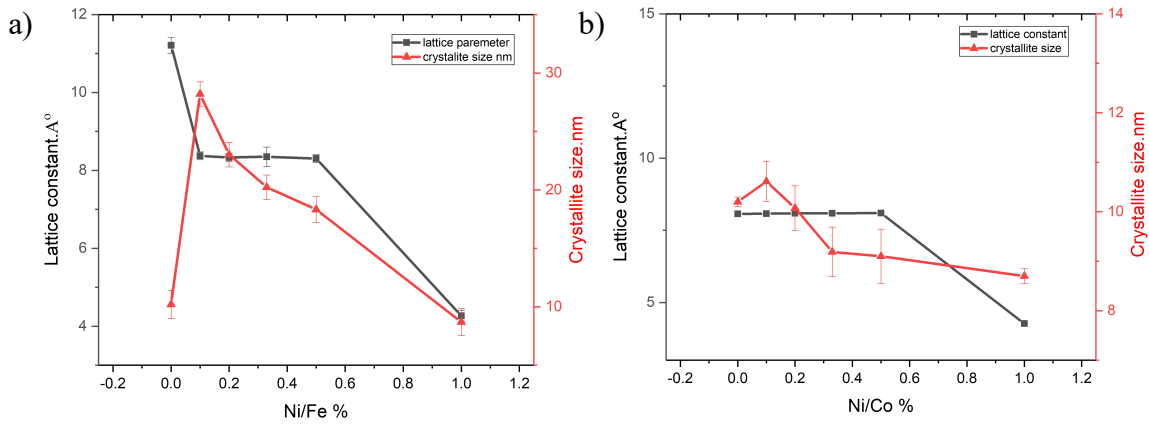
Figure 3 Lattice parameter and crystallite size obtained by Rietveld refinement of XRD scans as a function of a) Ni/Fe % and b) Ni/Co %.

Figure 3.b shows lattice constant and crystallite size vs Ni/Co%. Rietveld analysis was also used to find the crystallite size. the crystallite size decrease with increasing fraction of Ni/Co%. The crystalline size of the $NiCo_2O_4$ nanostructure was around 10 nm in agreement with recently reported for co-precipitated $NiCo_2O_4$ (6).

Raman spectroscopy represents a nondestructive material investigation technique, which is sensitive to structural disorder. Raman spectroscopy can distinguish crystalline nanoparticles smaller than 4 nm and amorphous phases that cannot be identified by XRD. (16).
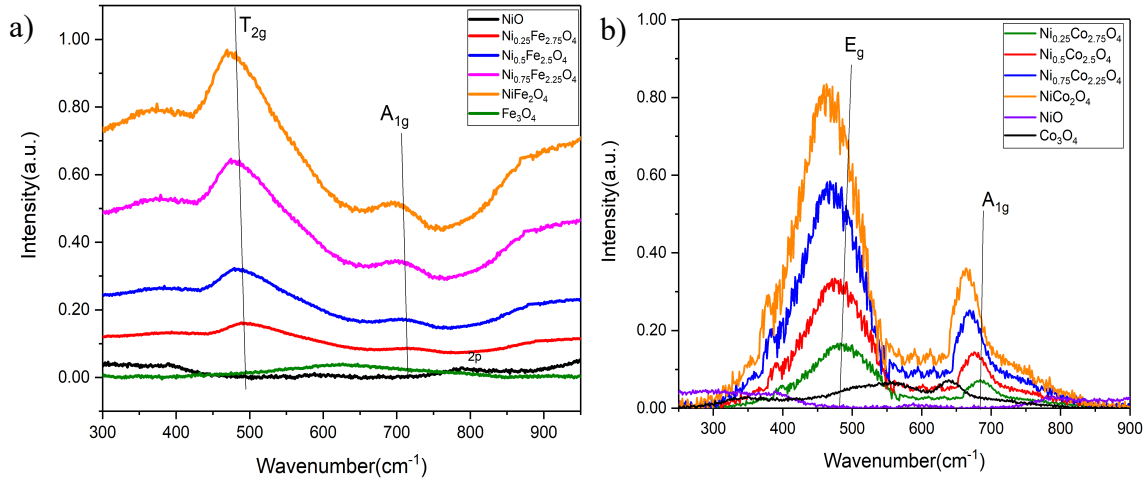
Figure 4 Raman Spectrum of a) $Ni_xFe_{3-x}O_4$ and b) $Ni_xCo_{3-x}O_4$ prepared by co-precipitation method and effect of Ni/Fe% and Ni/Co% concentration.

In Figure 4.a, while NiO has weaker Raman band at 900 cm^{-1}, $Ni_xFe_{3-x}O_4$ crystallize in a spinel structure of space group Fd-3m which resulted in five Raman active bands namely $A_{1g} + E_g + 3T_{2g}$ (16). In cubic ferrites, the strongest modes above 600 cm^{-1} correspond to symmetric stretching of oxygen in tetrahedral AO_4 groups, (17) so the modes at 690 cm^{-1} in the case of $NiFe_2O_4$ can be considered due to A_g symmetry (18). The mode T_{2g} at 470 cm^{-1} correspond to the vibrations of the octahedral group: T_{2g} is due to asymmetric stretching of oxygen (19-20).

Raman and XRD detect the $NiFe_2O_4$ presence in the bulk phase of the Ni-Fe oxide. Since Raman is extremely sensitive to small Fe oxide nanoparticles. The absence of Raman bands from iron oxide phases, especially the strong bands from α- Fe_2O_3, suggest that a separate Fe oxide phases are not detected in produced compounds (21,22). Figure 4.b displays the Raman spectra of $Ni_xCo_{3-x}O_4$, $NiCo_2O_4$ shows peaks at 467 and 672 cm^{-1}, which are due to E_g and A_{1g} vibrational modes of $NiCo_2O_4$ respectively. These two peaks are mainly identified and linked with Ni–O and Co–O vibrations of the spinel $NiCo_2O_4$ (23). Figure 5 shows Raman peak shift to lower wavenumbers as Ni/Fe % and Ni/Co % content increases. Wavenumber shift is specific to the chemical bonds and symmetry of molecules. Based on literature, there are some arguments can be considered to explain this wavenumber shift, The first is mass effect due to the change in the mass of dopant and host atoms, the second is the size effect due to the diversity in ionic radius of dopant and host atoms and the third is the force-constant change and bond strength as a result of chemical nature distinction between dopant and host atoms (24).
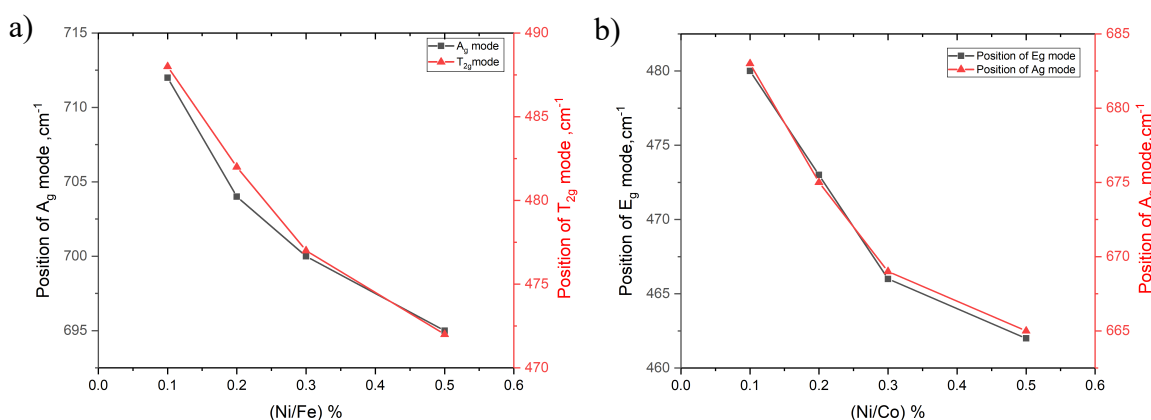

Figure 5 a) Shift peak positions of A_g and T_{2g} modes depending on x of $Ni_xFe_{3-x}O_4$ b) Shift peak positions of A_g and E_g modes depending on x of $Ni_xCo_{3-x}O_4$

An interesting phenomenon was found after measuring the BET surface area of oxide samples. Figure 6 indicates the relationship between Ni/Co% and Ni/Fe % vs BET surface area. BET surface area of NiFe and NiCo based oxides increases with increasing metal dopant concentration till reaching Ni/Co% and Ni/Fe% =0.5, which could be related deformation caused by dopant in the lattice of host oxide (25) and a decrease of crystallite size calculated from XRD measurements. While for NiO at x = 1, BET surface area decreases till reach around 29 m^2/gm. NiCo-oxides have nearly twice the BET surface area of NiFe-oxides produced by the same coprecipitation method. Therefore, we can argue that the higher surface area towards higher Ni-content in oxides favors HER due to an increased number of electrolyte accessible sites (26). Figure 6 BET surface area and respective calculated BET particle size of a) $Ni_xFe_{3-x}O_4$ and b) $Ni_xCo_{3-x}O_4$ prepared by co-precipitation process.

The average particle size (considering the particle is spherical and non-porous) by using BET.

$$SSA (BET) = 6 / (\rho \times D)$$

Where SSA [m^2/g] is the specific surface area measured by BET, ρ is the density of particles, and D is the particle diameter (26). BET particle size decreases and BET surface area increases along with Ni/Fe % and Ni/Co% increase till reach 0.5 %. BET surface area values are in good agreement with results from XRD measurements.
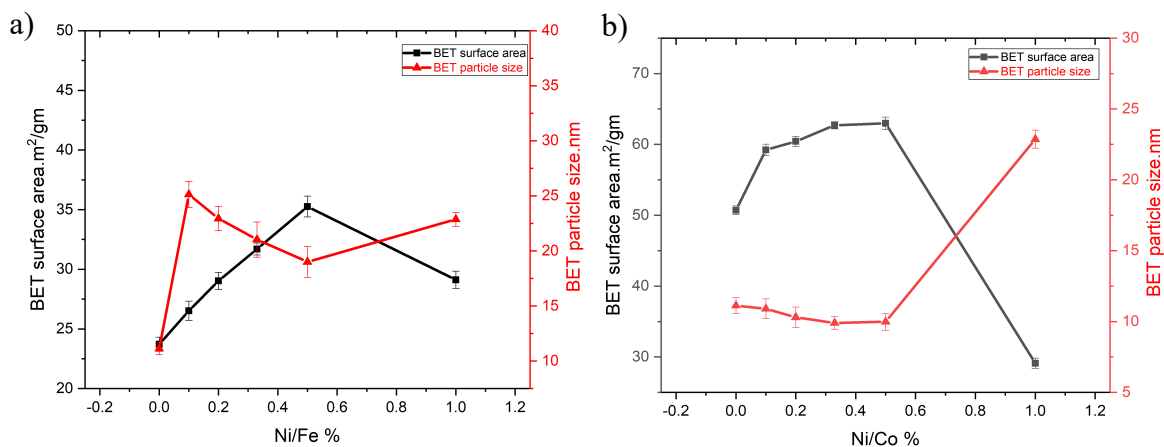

Figure 6 BET surface area and respective calculated BET particle size of a) $Ni_xFe_{3-x}O_4$ and b) $Ni_xCo_{3-x}O_4$ prepared by co-precipitation process.

Figure 7 shows the electrochemical performance of $Ni_xFe_{3-x}O_4$ and $Ni_xCo_{3-x}O_4$ obtained in N_2-saturated 0.1 M KOH at a rotation rate of 1600 rpm. All the data presented are the consistent ones obtained after the repetitive LSV experiments, i.e. after the stable cathodic activation. Figure 7.a and 7.b show LSV curves normalized to the geometric surface area of the electrode (glassy carbon with 5 mm diameter). As can be seen in Figure 7.a and 7.b, $NiFe_2O_4$ and $NiCo_2O_4$ have the lowest onset potential of 200 mV for HER in 0.1 M KOH. While bare Fe_3O_4 and NiO have 400 mV and 280 mV respectively. Onset potential value of nanoparticle catalysts is comparatively lower than observed for Vulcan x72 (1.01 V) and bare GC electrode (1.1 V) (27).

The rapid increase in the cathodic current was associated with the oxide reduction (28). Both the modified electrodes clearly showed an increment in the magnitude of current and potential shift with respect to the bare electrode GC or Vulcan x72 bare electrode, which confirms the electrocatalytic activity of NiFe and NiCo oxides towards HER (26-27). The enhanced electrocatalytic behavior of the oxide materials might arise from the synergetic effect of the exposed active sites provided by the ferrite, cobaltite oxide which in turn could enhance electron transport properties (29-32).

Figure 7.e and 7.f show HER activity normalized to the geometric surface area as a function of x in $Ni_xFe_{3-x}O_4$ and $Ni_xCo_{3-x}O_4$. Below x=0.5 the current density increases as the percentage of nickel increases but decreases beyond x=0.5 for a given applied overpotential. $NiFe_2O_4$ achieves -10 mA/cm^2 at an overpotential of 330 mV which has higher activity than NiFe NPs reported by Kumar et al. (27), while $NiCo_2O_4$ requires 317 mV to achieve the same current density. Figure 7.c and 7.g show LSV curves after normalizing the measured currents to the catalysts' BET surface areas. The specific activity of $NiFe_2O_4$ was 0.1 mA/cm^2_{BET} at an overpotential of 350 mV which was better than NiO and Fe_3O_4 with 0.1 mA/cm^2_{BET} at an overpotential of 450 mV.

Apparently, the composition of $Ni_xFe_{3-x}O_4$ influences electrocatalytic activity as shown in Figure 7.c. The overpotential η required to achieve 0.1 mA/cm²$_{BET}$ decreases as Ni/Fe % increase, $Ni_{0.25}Fe_{2.75}O_4 > Ni_{0.5}Fe_{2.5}O_4 > Ni_{0.75}Fe_{2.25}O_4 > NiFe_2O_4$. These results indicate the role of Ni/Fe% and BET surface area in providing more active sites for HER. Figure 7.d and 7.h shows the specific activity of $Ni_xCo_{3-x}O_4$. It's clear that the composition influences electrocatalytic activity and $NiCo_2O_4$ has the highest specific activity 0.1 mA/cm²$_{BET}$ at an overpotential of 404 mV.

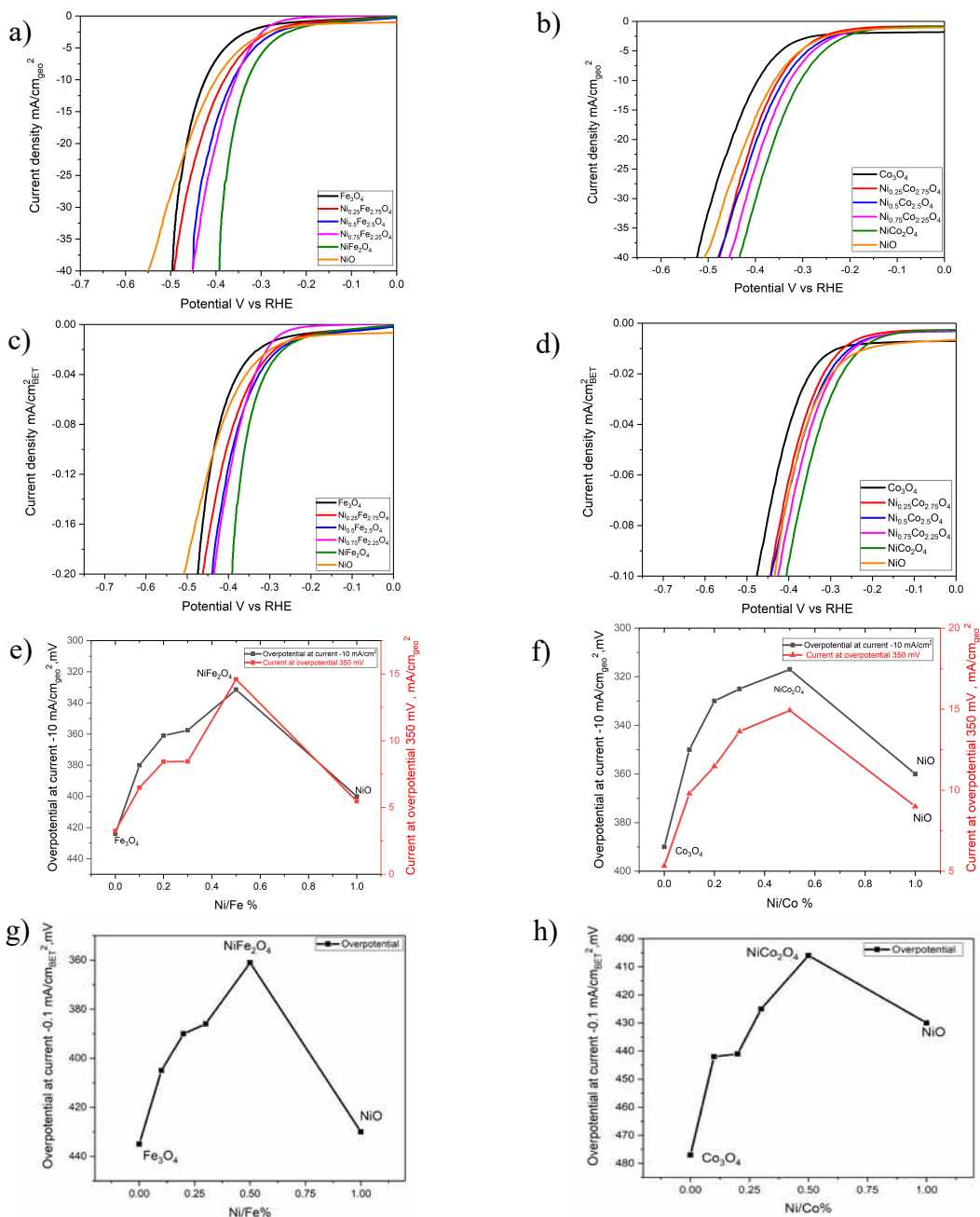Figure 7 Linear sweep voltammetry (LSV) normalized to geometric surface area of a) $Ni_xFe_{3-x}O_4$ b)$Ni_xCo_{3-x}O_4$ with corresponding activity merit in e and f respectively and LSVs normalized to BET surface area of c) $Ni_xFe_{3-x}O_4$ d)$Ni_xCo_{3-x}O_4$ with corresponding activity merits in g and h respectively, data obtained in N_2-saturated 0.1 M KOH with a rotation rate of 1600 rpm.

Tafel plots obtained from LSV curves, the plot of overpotential versus log current density (η vs. log j) are shown in Figure 8.a and 8.b, which could be exploited for the quantitative kinetics analysis of HER. The linear regions of the Tafel plots were fitted into the Tafel equation

$$\eta = a + b \log i$$

where b is Tafel slope. Tafel Slope close to 120 mV dec^{-1} indicating HER rate-determining step is electrochemical adsorption. $NiFe_2O_4$ and $NiCo_2O_4$ show a relatively small Tafel slope of 130 and 125 mV dec^{-1}. The lower overpotential and lower Tafel slope demonstrate that $NiFe_2O_4$ and $NiCo_2O_4$ have better HER catalytic activity than other $Ni_xFe_{3-x}O_4$ and $Ni_xCo_{3-x}O_4$. Figure 8.c and 8.d shows Tafel impedance as extracted from EIS measurements at a specific overpotential of -200 mV. For the sake of clarity, the spectrum is plotted as Tafel impedance Z_t (i.e. impedance multiplied with the steady-state current density) (33).

$$Z_t = (\tilde{E}/\tilde{i}) * i_{st}$$

Where i_{st} the steady-state current density, $\tilde{E}$ is the potential amplitude and $\tilde{i}$ is the current density amplitude (taken here to be positive). The solution resistance has been subtracted from all data, solution resistance determined from the high-frequency intercept of the Nyquist plot with the real axis. For all samples, the diameter of the arc in the Tafel-impedance plane plot are in good agreement with the Tafel slopes from the steady-state polarization curves (34). Tafel impedance displays a high-frequency tail due to electrode polarization owing to the formation of $Ni(OH)_2$ layer (35).
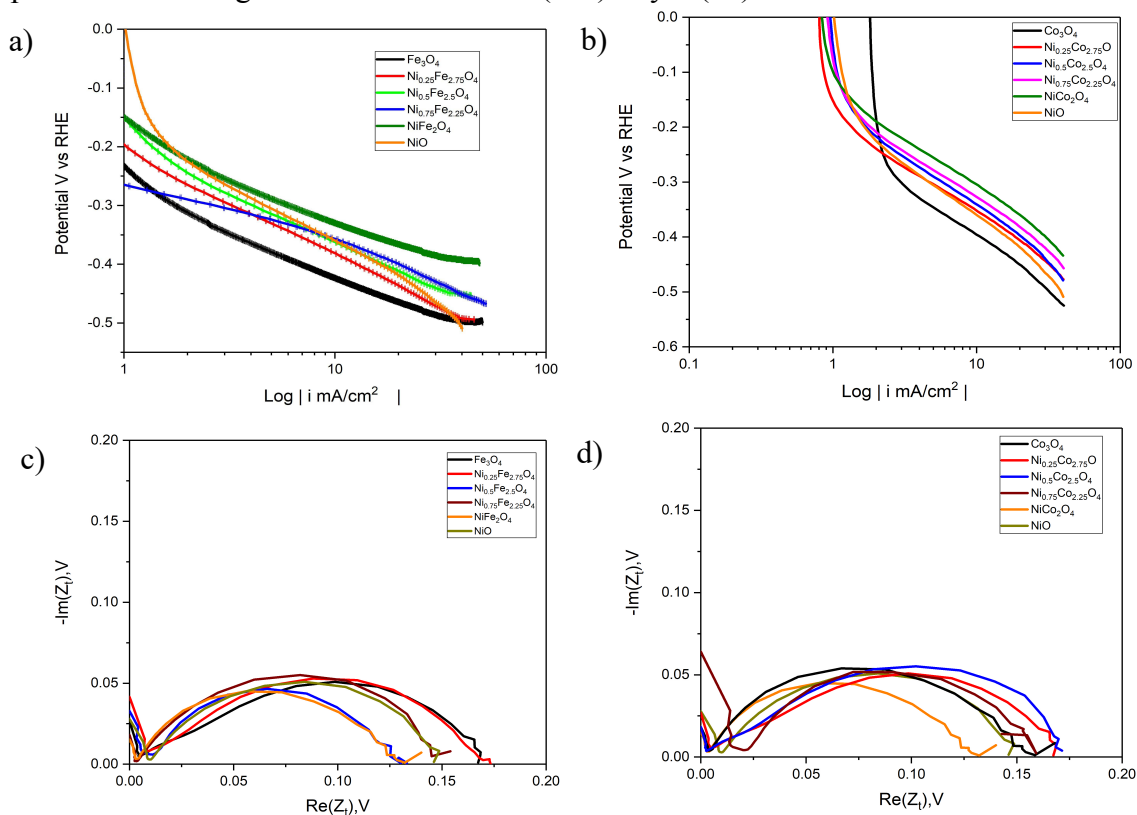

Figure 8 Tafel plot resulted from LSV measurements a) $Ni_xFe_{3-x}O_4$ b) $Ni_xCo_{3-x}O_4$, and Tafel impedance of c) $Ni_xFe_{3-x}O_4$ d) $Ni_xCo_{3-x}O_4$ at overpotential -200 mV, obtained in N_2-saturated 0.1 M KOH with a rotation rate of 1600 rpm.

Electrochemical impedance spectroscopy (EIS) investigates hydrogen adsorption kinetics on the catalyst's surface and its evolution from the surface. Figure 9.a and 9.c shows the Nyquist plots of $NiFe_2O_4$ and $NiCo_2O_4$ at different applied potentials (−150 to −300 mV vs RHE). At higher applied potential, the radius of the semicircle decreases, signifying a lower charge transfer resistance (R_{ct}) and a higher rate of hydrogen evolution (36-38).

$NiCo_2O_4$ nanoparticles exhibit a R_{ct} value of 100 Ω at an applied potential of -350 mV. While $NiFe_2O_4$ were found to exhibit charge transfer resistances of 120 Ω. As displayed in Nyquist plot, The faster electron transfer of $NiCo_2O_4$ as compared to that of $NiFe_2O_4$ is due to the reduction of charge transfer resistances, suggesting high electronic conductivity of $NiCo_2O_4$ during the electrochemical reaction and enhanced electrocatalytic activity (33).

From Figure 9.b and 9.d, the Bode diagram indicates that the value of the maximum phase angle decreases and the frequency at the maximum shifts to higher values at higher applied potential. This suggests faster kinetics of the hydrogen evolution reactions. Bode plot also shows a onetime constant process in both $NiFe_2O_4$ and $NiCo_2O_4$ (39).
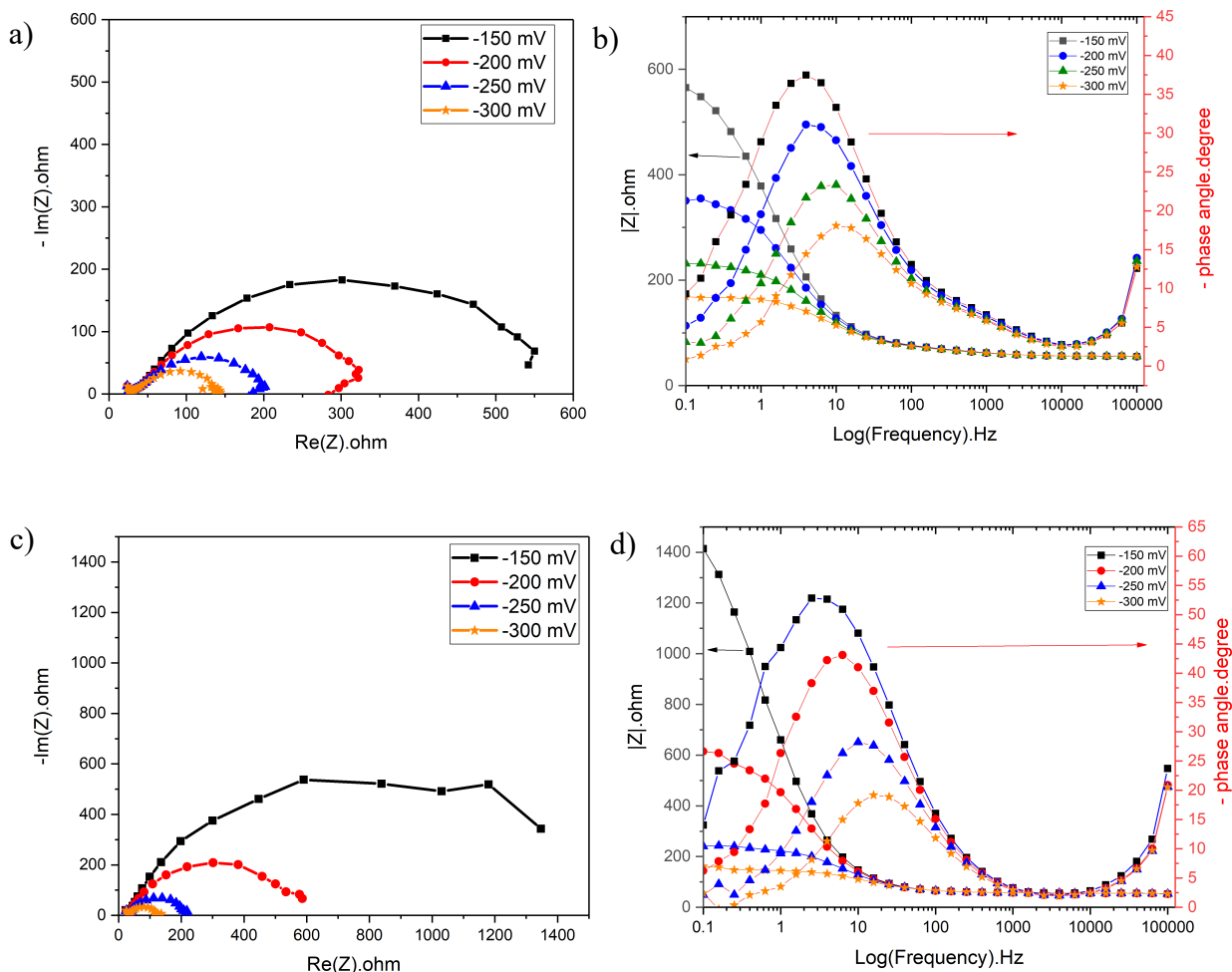

Figure 9 Electrochemical impedance spectroscopy (EIS) measurement: (a), (B) Nyquist plots and Bode plots of $NiFe_2O_4$ respectively, c) and (d) Nyquist plots and Bode plots of $NiCo_2O_4$ at different applied bias potentials (−150 to −300 mV vs RHE) respectively.

Stability is an important criterion for a good catalyst as the cost of hydrogen is directly proportional to the lifetime of the catalyst. $NiFe_2O_4$ and $NiCo_2O4$ were chosen for durability measurements as they possess the highest electrochemical activity. To check the stability of $NiFe_2O_4$, LSV curves before and after chronoamperometry for 20 hours at a fixed overpotential of -350 mV was carried out. From figure 11.a, chronoamperometry current density at -350 mV corresponding to the results obtained from LSV for the same applied overpotential. In Figure 10.a, the serrated shape time-dependent current density curve observed is attributed to the accumulation and release of hydrogen bubbles. Bubbles impede efficient contact between catalyst and electrolyte. The sharp increase in resulted current density after 2 hours is due to the reduction of oxides in electrocatalyst powder. In figure 10.b, there is only a change of 22 mV in the overpotential at a current density of -10 mA cm^{-2} from LSV before and after chronoamperometry measurements, This indicates that $NiFe_2O_4$ exhibits good stability during hydrogen evolution in alkaline media (34,35). In Figure 10.c, to test the stability of $NiCo_2O_4$, LSV measurements have been carried out before and after 1000 cycles, the polarization curves showed its high durability for HER catalysis with a small shift in overpotential to achieve the same current density.
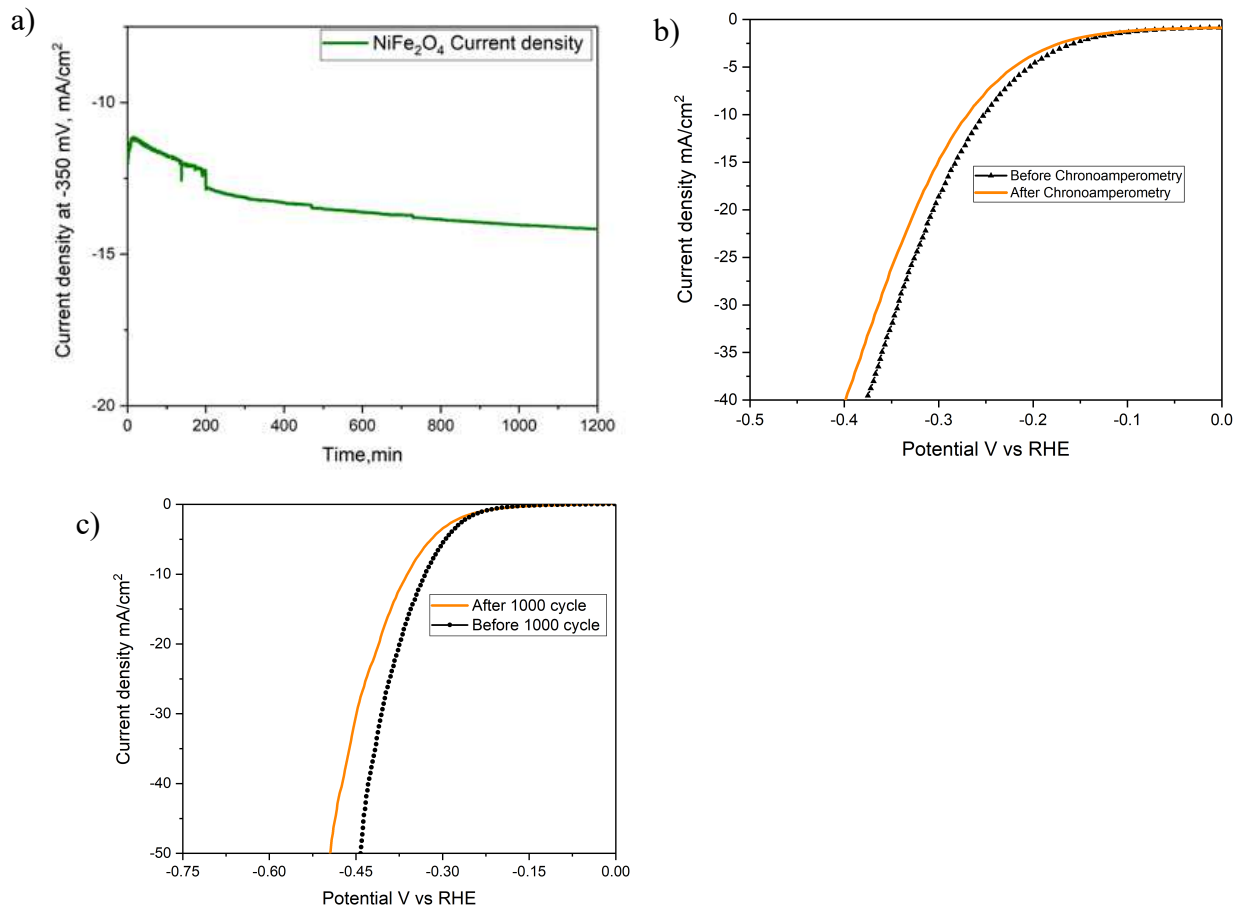

Figure 10 a) chronoamperometry of $NiFe_2O_4$ in 0.1 M KOH b) LSV before and after chronoamperometry measurement of $NiFe_2O_4$ c) LSV before and after 1000 cycle of $NiCo_2O_4$.
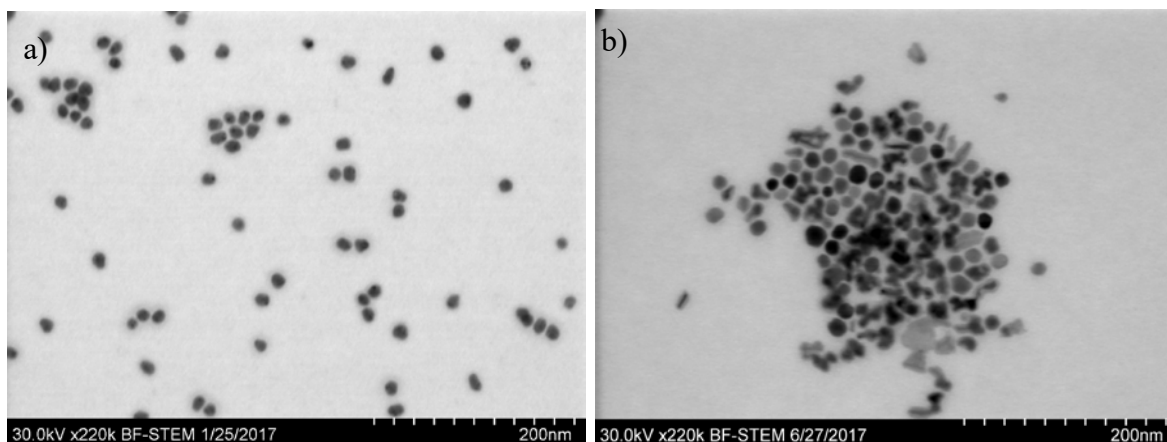
Thermal reduction by Oleylamine

Figure 11 SEM images of a) NiCo, b) NiFe nanoparticles produced from Thermal reduction by oleylamine.

Size and morphology of nanoparticles resulted from thermal reduction by oleylamine were investigated by Hitachi S500 FESEM, Figure 11 displays a representative SEM image of the products obtained from the typical synthesis of NiCo and NiFe nanoparticles. thermal reduction of Ni(acac)$_2$ and co(acac)$_2$ by oleylamine produce homogeneous nanoparticle morphology, NiCo nanoparticles has an average nanoparticle diameter of 12 ± 3.5 nm, while thermal reduction of Ni(acac)$_2$ and Fe(acac)$_3$ by oleylamine produce nanoparticle and nanoplates morphology. NiFe nanoparticles have an average nanoparticle diameter of 15 ± 4.5 nm and NiFe nanoplates length is about 27 ±10 nm.

Using open source software (image J), particle size estimated from high-resolution STEM images and assuming spherical particles we employed the following equation for the overall surface area $S_{overall}$ (33)

$$S_{overall} = 6 \times 10^3 / (\rho \times d)$$

where ρ = 8.9 and 8.38 gcm^{-3} is the density of NiCo, NiFe respectively and d is the particle size.

Table 2 particle diameter and calculated surface area of NiCo and NiFe.

Alloy	Particle diameter, nm	Surface area, m^2/gm
NiCo	12 ± 3.5 nm	56.1 ± 2.1
NiFe	15 ± 4.5	47.73 ± 1.84

It can be seen from Table 2 that NiCo nanoparticles possess higher overall surface area than NiFe nanoparticles. This clearly due to a lower particle size of NiCo compared to NiFe nanoparticles.
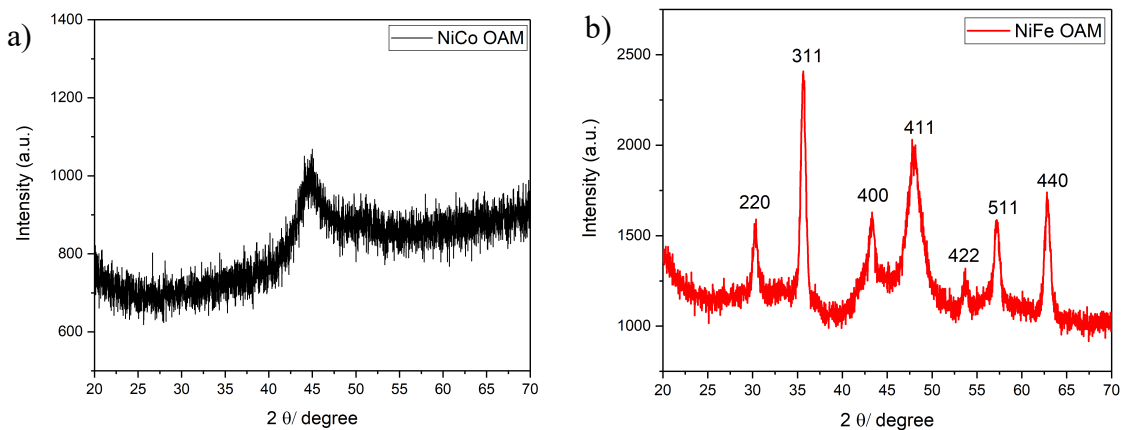
Figure 7 XRD pattern of a) NiCo and b) NiFe prepared by thermal reduction using oleylamine.

XRD pattern for NiCo prepared through thermal reduction using oleylamine (OAM) in figure 12. NiCo shows amorphous nature with a very broad peak at 45° due to low particle size. XRD pattern of NiFe nanoparticles shows the presence of $NiFe_2O_4$. The diffraction peaks at 2θ values of 30.11°, 35.57°, 42.91°, 48.2°, 53.33°, 57.11°, and 62.61° can be attributed to the crystalline planes of (220), (311), (400), (441), (422), (511), (440), respectively. These peaks belong to spinel $NiFe_2O_4$ with JCPDS no. 86-2267 (11-12).
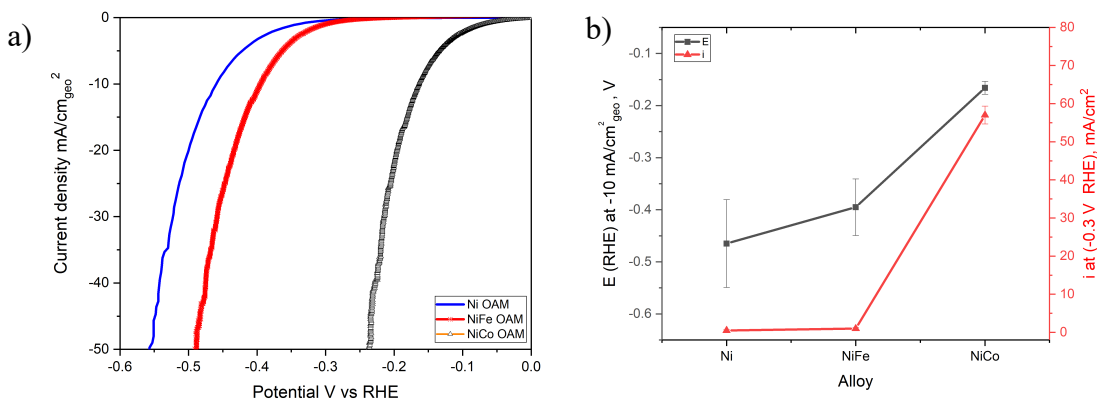

Figure 13.a) LSV of Ni, NiFe and NiCo nanoparticles b) potential at -10 mA/cm^2 and current at -0.3 V for HER activity of Ni, NiFe and NiCo nanoparticles catalysts in 0.1 M KOH (N$_2$-purged) at 1600 rpm.

Electrochemical hydrogen evolution reactions of NiCo, NiFe nanoparticles were investigated in 0.1 M KOH aqueous solution using a typical three-electrode system, where a modified glassy carbon electrode and Hg/HgO electrode were used as the counter and reference electrodes, respectively. Linear sweep voltammetry (LSV) studies in Figure 13.a and 13.b demonstrate that NiCo nanoparticles show the highest HER activity, with a maximum current density of 50 mA cm^{-2} at an overpotential of 240 mV. NiCo nanoparticles require overpotential of -150 mV to drive current density of -10 mA/cm^2, compared to NiFe and Ni nanoparticles that require a higher overpotential of 390 and 460 mV respectively to achieve a current density of -10 mA/cm^2.
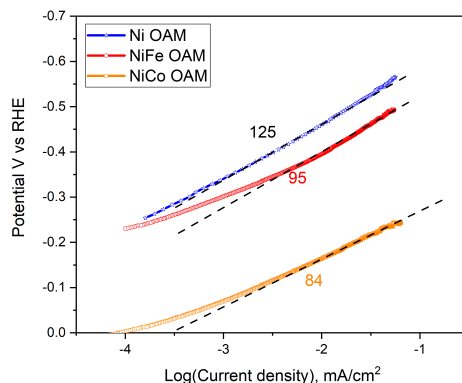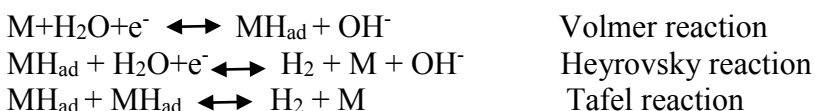
Figure 14 Tafel plot calculated from the LSV curve of Ni. NiFe and NiCo nanoparticles in 0.1 M KOH (N₂-purged) at 1600 rpm.

Tafel slopes reflect an inherent property of the HER catalysts, determination of the reaction mechanism of the HER and the process rate determining step (RDS) can be attained using Tafel analysis. The overall reaction proceeds via two possible reaction pathways: Volmer–Heyrovsky and Volmer–Tafel. Volmer reaction involves electroreduction of water molecules with hydrogen adsorption; while Heyrovsky reaction involves electrochemical hydrogen desorption, and Tafel reaction involves chemical desorption (34).

$M+H_2O+e^- \longleftrightarrow MH_{ad} + OH^-$ Volmer reaction
$MH_{ad} + H_2O+e^- \longleftrightarrow H_2 + M + OH^-$ Heyrovsky reaction
$MH_{ad} + MH_{ad} \longleftrightarrow H_2 + M$ Tafel reaction

The kinetic parameters for the HER (j_o and b) for the investigated systems were derived from Tafel equation:

$$\eta = a + b \log j$$

where η (V) is the applied overpotential, j (mA.cm^{-2}) is the current density, b (V dec^{-1}) the Tafel slope and a (V) the intercept. This intercept is related to the exchange current density j_o, through equation (34):

$$a=(2.3*RT)/(\beta nF) * \log j_o \qquad b=(2.3*RT)/(\beta nF)$$

where R is the gas constant (8.314 kJ mol^{-1} K^{-1}), β is the symmetry factor, n is the number of electrons exchanged and F is the Faraday constant (96,485 ∘C mol^{-1}). results are presented in Table 3. Herein. The linear regions of Tafel plots in figure 14 were fitted to the Tafel equation, yielding Tafel slopes of 125, 95 and 84 mV/dec for Ni, NiFe, and NiCo respectively. The rate controlling step is a Volmer reaction as the obtained Tafel slope is close to 120 mV dec^{-1}. The Tafel values of the Ni. NiFe and NiCo, display the reaction mechanism of catalysts for HER occur through a Volmer–Tafel mechanism (36).

Table 3 Overpotential at -10 mA/cm², the current density at – 300 mV, Tafel slope b, log J$_o$ and exchange current density j$_0$ for investigated catalysts in 0.1 M KOH.

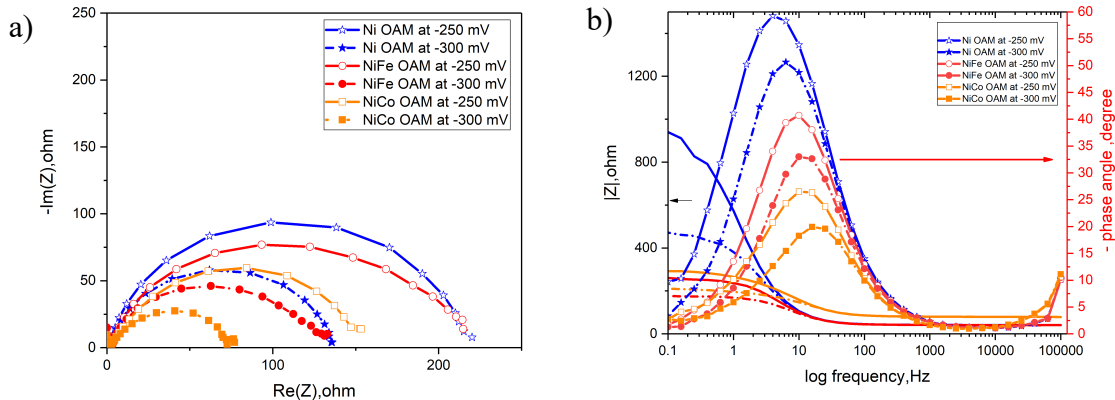| Catalyst	Overpotential (V) at -10 mA/cm²	Current density at -300 mV	Tafel Slope mV/decade	Log J$_o$ (A/cm²)	J$_o$ (A/cm²)
Ni OAM	-0.465	0.5	125	5.9	1.26*10⁻⁶
NiFe OAM	-0.395	1	95	5.2	6.3*10⁻⁶
NiCo OAM	-0.166	57	84	3.7	2 *10⁻⁴

Figure 15 Electrochemical impedance spectroscopy (EIS) measurement:(a) Nyquist plots and (b) Bode plots of Ni, NiFe and NiCo nanoparticles at different applied bias potentials (-250 to -300 mV vs RHE) in 0.1 M KOH (N_2-purged) at 1600 rpm.

Electrochemical impedance spectroscopy (EIS) was carried out for further investigation of the electrode kinetics and electrode-electrolyte interface. Figure 15.a shows the Nyquist plots of Ni, NiFe, and NiCo at different applied potentials (-250 to -300 mV vs RHE). At higher applied potential, the radius of the semicircle decreases, signifying a lower charge transfer resistance (R_{ct}) and a higher rate of hydrogen evolution. also, NiCo nanoparticles exhibit R_{ct} value of 76 Ω at an applied potential of -300 mV. Which further confirm the reason for superior activity of NiCo nanoparticles, However, Ni and NiFe were found to exhibit high charge transfer resistances of 138 and 141Ω, respectively, From the Bode diagram in figure 15.b, it is observed that the value of the maximum phase angle decreases and the frequency at the maximum shifts to higher values at higher applied potential. NiCo nanoparticles behave the lowest phase angle at a higher frequency, this suggests faster kinetics of the hydrogen evolution reactions (38).

Conclusions

In summary, this work demonstrates a cheap, stable and environmentally favorable nanocatalyst for Hydrogen evolution reaction in alkaline electrolysis. Nanocatalysts were synthesized by a simple co-precipitation and thermal reduction methods. Different compositions of $Ni_xFe_{3-x}O_4$ and $Ni_xCo_{3-x}O_4$ were investigated using co-precipitation method. Raman and XRD data confirmed the presence of $NiFe_2O_4$ and $NiFe_2O_4$ spinel oxide in the catalyst. $NiFe_2O_4$ and $NiFe_2O_4$ have the lowest crystallite size and the highest BET surface area. $NiCo_2O_4$ represent the highest electroactivity towards HER which requires 317 mV to achieve -10 mA/cm^2, while $NiFe_2O_4$ requires overpotential of 330 mV to achieve the same current density. NiCo metallic nanoparticles prepared via thermal reduction by oleylamine, have a small particle size and amorphous nature. NiCo has the lowest Tafel slope of 84 mV/decade and achieves -10 mA/cm^2 with 166 mV applied overpotential, compared to Ni and NiFe which have much higher Tafel slope and require higher overpotential of 465 and 395 mV to achieve the same current density.

Acknowledgments

References

1. J. Durst et al., Energy Environ. Sci., 7, 2255–2260 (2014).
2. F. M. Sapountzi, J. M. Gracia, C. J. Kee. J. Weststrate, H. O. A. Fredriksson, and J.W.Hans, Prog. Energy Combust. Sci., 58, 1–35 (2017).
3. J. R. Varcoe et al., Energy Environ. Sci., 7, 3135–3191 (2014).
4. W. Sheng, H. A. Gasteiger, and Y. Shao-Horn, J. Electrochem. Soc., 157(11), B1529-B1536 (2010).
5. Vincent, I. & Bessarabov. Renew. Sustain. Energy Rev. 81, 1690–1704 (2018).
6. D. Chanda, J. Hnát, T. Bystron, M. Paidar, and K. Bouzek, J. Power Sources, 347,247–258 (2017).
7. D. Wang and D. Astruc, Chem. Soc. Rev, 46, 816–854 (2017).
8. J. Wang et al., ACS Appl. Mater. Interfaces, 9, 7139–7147 (2017).
9. D. Chanda, J. Hnát, M. Paidar, J. Schauer, and K. Bouzek, J. Power Sources, 285,217–226 (2015).
10. Silambarasan. M. et al, in Recent Trends in Materials Science and Applications. J.Ebenezar, Jeyasingh, Editors, p.492,Springer Proceedings in Physics(2017).
11. R. Nivetha et al., J. Magn. Magn. Mater. 448, 165-171 (2017).
12. U. Kurtan, H. Erdemi, A. Baykal, and H. Güngüneş, Ceram. Int, 42, 13350–13358(2016).
13. Y. Ma et al., ACS Appl. Mater. Interfaces, 8, 34396–34404 (2016).
14. G. Gupta, K. Scott, and M. Mamlouk, J. Power Sources, 375, 387–396 (2018).
15. C. Chang, L. Zhang, C.-W. Hsu, X.-F. Chuah, and S.-Y. Lu, ACS Appl. Mater.Interfaces, 10 (1), 417–426 (2018).
16. K. Fominykh et al., Adv. Funct. Mater. 27, 1605121(2017).
17. A. Ahlawat and V. G. Sathe, J. Raman Spectrosc, 42, 1087–1094 (2011).
18. Z. Ž. Lazarević et al., J. Appl. Phys, 113, 187221 (2013).
19. J. Landon, Ethan Demeter et al., ACS Catal., 2, 1793–1801 (2012).
20. J.-Q. Chi et al., Int. J. Hydrogen Energy, 42, 20599–20607 (2017).
21. G. Liu, K. Wang, X. Gao, D. He, and J. Li, Electrochimica Acta, 211, 871–878 (2016).
22. N. Mironova-Ulmane et al., J. Phys. Conf. Ser., 93 (2007).
23. Y. Xiao et al., J. Mater. Chem. A, 5, 15901–15912 (2017).
24. H. K. Yadav, K. Sreenivas, V. Gupta, and R. S. Katiyar, J. Raman Spectrosc, 40,381–386 (2009).
25. J. B. Condon, measurements and Theory, p. 1689-1699, (2013).
26. M. Gorlin et al., J. Am. Chem. Soc, 139, 2070–2082 (2017).
27. A. Kumar and S. Bhattacharyya, ACS Appl. Mater. Interfaces, 9, 41906–41915(2017).
28. H. Chen, J. Yan, H. Wu, Y. Zhang, and S. Liu, J. Power Sources, 324, 499–508(2016).
29. V. Vij et al., ACS Catal, 7, 7196–7225 (2017).
30. J. Liu, D. Zhu, T. Ling, A. Vasileff, and S. Z. Qiao, Nano Energy, 40, 264–273(2017).
31. L. Fang et al., J. Catal, 357, 238–246 (2018).
32. S. Debata, S. Patra, S. Banerjee, R. Madhuri, and P. K. Sharma, Appl. Surf. Sci.(2018),https://doi.org/10.1016/j.apsusc.2018.01.302
33. M. Darab, A. O. Barnett, G. Lindbergh, M. S. Thomassen, and S. Sunde, Electrochimica Acta, 232, 505–516 (2017).

34. E. A. Franceschini, G. I. Lacconi, and H. R. Corti, Electrochim. Acta, 159, 210–218 (2015).
35. Ibrahim Dincer, Comprehensive Energy Systems, p.5540, Elsevier (2018).
36. V. M. Nikolic et al., Appl. Catal. B Environ., 179, 88–94 (2015).
37. A. Mukherjee, S. Chakrabarty, W.-N. Su, and S. Basu, Mater. Today Energy, 8, 118–124 (2018).
38. K. Ojha, S. Saha, S. Banerjee, and A. K. Ganguli, ACS Appl. Mater. Interfaces, 9, 19455–19461 (2017).
39. Z. Grubač and A. Sesar, Croat. Chem. Acta, 90, 273–280 (2017).